Invisible Thin-Film Patterns with Strong Infrared Emission as an Optical Security Feature

Gokhan Bakan,* Sencer Ayas, Murat Serhatlioglu, Caglar Elbuken, and Aykutlu Dana

Spectrally selective thermal emission is in high demand for thermophotovoltaics, radiative cooling, and infrared sensing applications. Spectral control of the emissivity is historically achieved by choosing the material with suitable infrared properties. The recent advancements in nanofabrication techniques that lead to enhanced light–matter interactions enable optical properties like infrared emissivity that are not naturally available. In this study, thermal emitters based on nanometer-thick dielectrics on field-enhancement surfaces as optical security features are proposed. Such a function is achieved by generating patterns by ultrathin dielectrics that are transparent in the visible and exhibit strong infrared absorption in the spectral range of thermal cameras. The invisible patterns are then revealed by thermal imaging. The field-enhancement surfaces enhance the emissivity of the patterns, in turn reduce the minimum temperature to detect the thermal emission down to ≈30 °C from >150 °C to exploit ubiquitous heat sources like the human body. The study provides a framework for the use of thermal emitters as optical security features and demonstrates applications on rigid and flexible substrates.

1. Introduction

Hot bodies radiate electromagnetic waves mainly in the infrared and visible ranges of the electromagnetic spectrum. The radiation spectrum is broad and its intensity increases with increasing surface temperature while the peak intensity

Prof. G. Bakan, Dr. S. Ayas, M. Serhatlioglu, Prof. C. Elbuken, Dr. A. Dana
UNAM Institute of Material Science and Nanotechnology
Bilkent University
Ankara 06800, Turkey
E-mail: gokhan.bakan@atilim.edu.tr

Prof. G. Bakan
Department of Electrical and Electronics Engineering
Atilim University
Ankara 06830, Turkey

Dr. S. Ayas
Canary Center at Stanford for Cancer Early Detection
Department of Radiology
Stanford School of Medicine
Palo Alto, CA 94304, USA

Dr. A. Dana
E. L. Ginzton Laboratory
Stanford University
Stanford, CA 94305, USA

The ORCID identification number(s) for the author(s) of this article can be found under https://doi.org/10.1002/adom.201800613.

blueshifts as described by the Planck's law. The broad spectrum is useful for illumination purposes in the visible and as well as in the infrared. On the other hand, spectrally selective thermal emission is desired for applications like thermophotovoltaics,[1–3] radiative cooling,[4,5] sensing,[6–8] and near-infrared communication[9,10] by modifying the emissivity of the surfaces. The emissivity of a surface is equal to its absorbance in thermal equilibrium according to the Kirchhoff's law of thermal emission, ranging from 0 for a perfect mirror to 1 for a perfect absorber or a blackbody. A simple approach to modify the emissivity is finding a dielectric with phonon bands at the desired absorption wavelength range. A recent example is embedding glass microspheres in an infrared transparent polymer matrix for radiative cooling.[11] The dielectric dimensions can be as thin as micrometers when a back mirror, typically an optically thick metal layer is employed. This approach has been preferred for selective thermal emission since early 1980s, e.g., using ≈1 µm thick silicon monoxide on Al for radiative cooling. Owing to the simplicity of the structure, surfaces consisting of polar-dielectric-coated mirrors are still popular.[12] Stacking more than one type of polar dielectric layers broadens the absorption bands, that is especially useful for radiative cooling.[13] Using single[14] or multiple[1,15] lossless, that is infrared transparent, layers together with polar dielectrics introduce additional design parameters, hence offers better thermal-emission tunability.

Despite the simplicity that the polar dielectrics offer, their emission spectra are limited with the absorption bands. An arbitrary emission spectrum can be achieved by optical resonators such as Salisbury screens that consist of a lossless dielectric layer between a bottom mirror and a thin lossy layer on the top.[16–19] The absorbance wavelengths (resonances) are mainly determined by the optical thickness of the lossless dielectric layer. Alternatively, the lossy dielectric can be coated directly on the mirror layer exhibiting strong interference effects.[20–22] The absorbance wavelengths in this case are primarily determined by the optical properties of the lossy layer and its thickness. The strong interference surfaces consist of a simple bilayer structure, but exhibit broad absorbance spectra. Nanostructured films of metal or lossy materials, e.g., micrometer-scale gratings,[23] photonic crystals,[24] antennas,[15,25,26] provide a better control over the emission spectrum at the expense of the ease of fabrication. The emitter design can be as complex

ADVANCED
SCIENCE NEWS
www.advancedsciencenews.com

ADVANCED
OPTICAL
MATERIALS
www.advopticalmat.de

as patterned photonic crystals atop the loss-less/lossy dielectrics stack to achieve the desired optical performance.[27] If the lossy layer exhibits tunable optical properties like graphene,[19,28] quantum dots,[29,30] or phase-change materials,[17,21,22,31,32] the emission spectrum can be dynamically controlled.
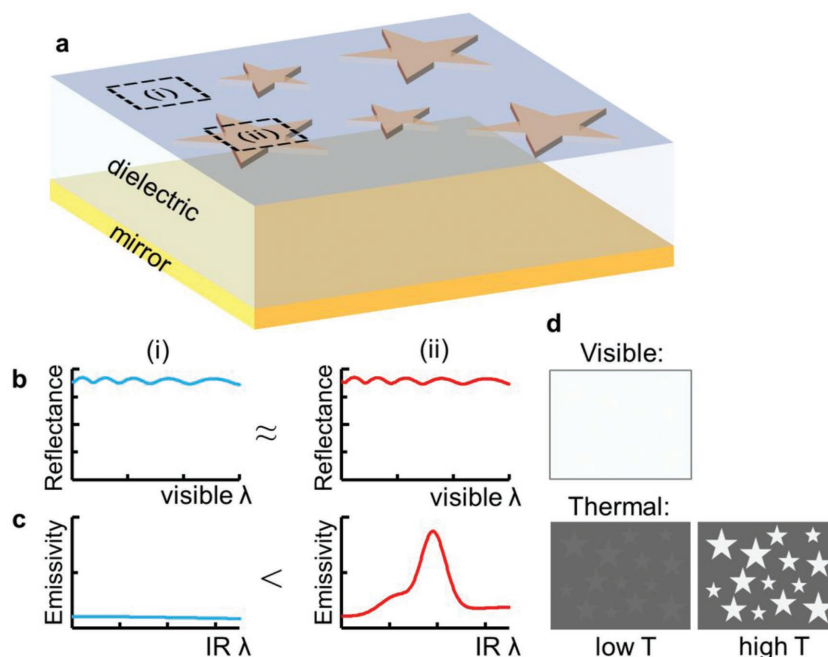
Among the aforementioned thermal emitter structures, the ones based on Salisbury screens exploit nanometer-thick absorber/emitter layers, thus present a unique opportunity for optical encryption-decryption applications by creating patterns that are imperceptible by the naked eye, or cameras, and emit detectable thermal radiation. Such a function defines a new application for thermal emitters that necessitate a new set of design requirements. This study provides a framework for thermal emitters as optical security features and demonstrates applications with various substrates and materials. The ease of fabrication on large-area, flexible substrates like Al foils and imaging by a low-cost smart-phone-attachment-type thermal camera using the external temperature of the human body surpasses the performances of the recent reports pursuing alternative approaches such as creating images using plasmonic structures and encrypting–decrypting the images by dynamically controlling the polarization of the incident light[26,33–35] or the optical properties of the structures.[36]
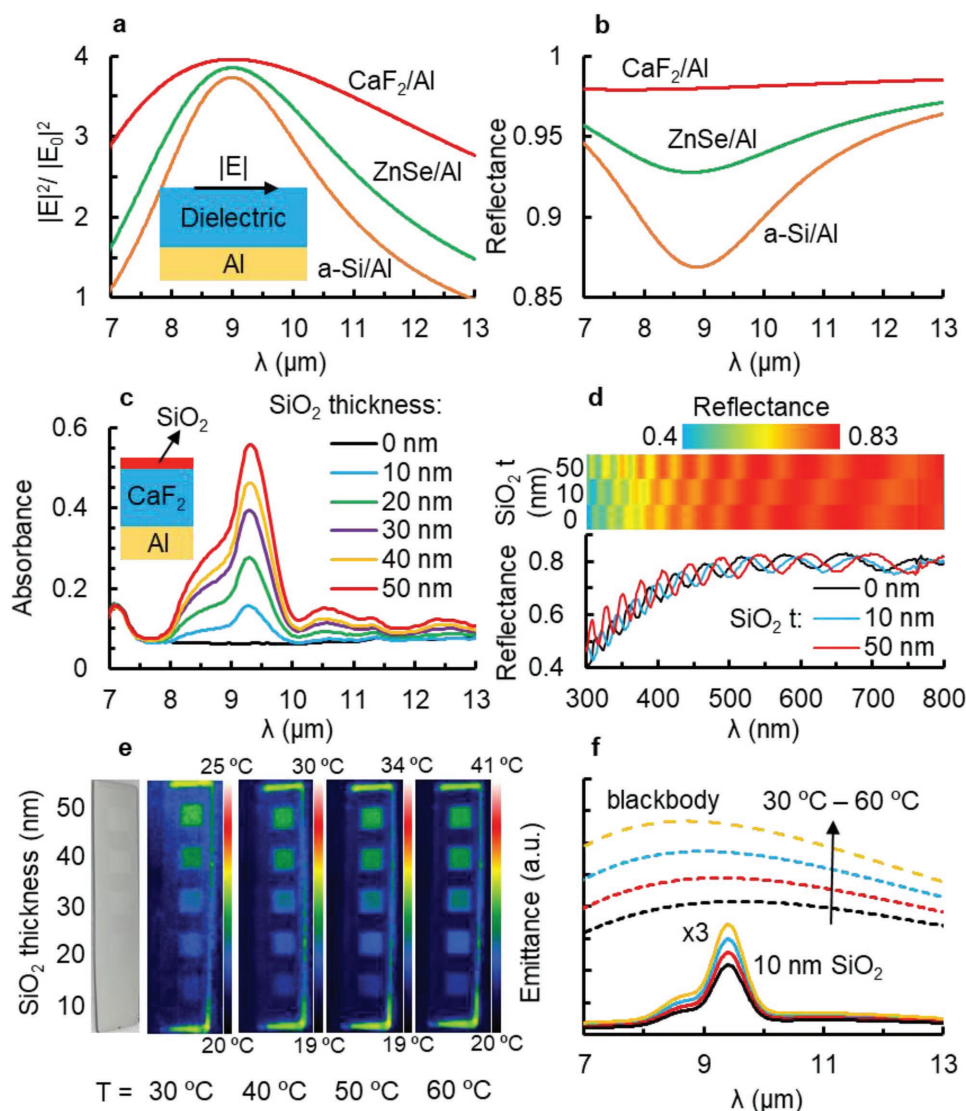

Figure 1. Working principle of the surfaces. a) 3D illustration of the surface. The star patterns are nanometer-thick films that are lossless in the visible, but lossy in the infrared. b) Example reflectance spectra in the visible and c) infrared absorbance/emissivity of i) the dielectric and ii) absorber/emitter surface. The effect of the emitter layer on the reflectance spectra in the visible regime must be unnoticeably small. Emissivity of the surface, on the other hand, must be small without the emitter layer and must be enhanced noticeably with the emitter layer. d) Illustrated top-down visible and thermal images.

2. Results

2.1. Designing the Surfaces

When an electromagnetic wave is incident on a perfect mirror, standing wave patterns are generated exhibiting periodic electric-field minima and maxima points. Introducing a thin absorber layer at the distance where the field is maximized forms a Salisbury screen and enhances the absorbance by the absorber layer by a factor of ≈ 4 compared to its absorbance suspended in air. The enhanced infrared absorbance by atop nanometer-thick films with the right choice of materials[37] has led to the idea of revealing the nanometer-thick films that are invisible to the naked eye by sensing their IR emission (**Figure 1**).

The emission from the surfaces depends on the emissivity and the surface temperature. It is desired to sense the patterns' IR emission close to room temperature ($\approx 30\ °C$) to make use of ubiquitous heat sources like the human body. Thus, the top absorber/emitter material must absorb/emit the IR light around $\lambda = 9.5\ \mu m$ that is the peak thermal emission wavelength for a blackbody at $30\ °C$. The emitter layer must also be optically thin ($n \times t$, where n is the refractive index and t is the thickness) and lossless in the visible such that its presence

cannot to be perceived in the visible. Thus, SiO_2 is chosen as the absorber/emitter layer due to its low refractive index in the visible, strong absorptivity in the wavelength range of 9–10 μm overlapping with the peak emission wavelength at 30 °C, and ease of deposition (Figure S1, Supporting Information). To enhance the absorbance of the infrared light by the top SiO_2 layer, the electric field within this layer, hence at the surface of the dielectric must be enhanced following the Beer's Law. The total electric field on the dielectric surface is the vector sum of electric fields of the incident and reflected rays. For normal incidence, the field-intensity enhancement factor ($|E|^2/|E_0|^2$) is

$$\left| 1 + \frac{r_{12} + r_{23}e^{2i\beta}}{1 + r_{12}r_{23}e^{2i\beta}} \right|^2 \tag{1}$$

where r_{12} is the reflection coefficient for the dielectric-air interface, r_{23} is the reflection coefficient for the metal-dielectric interface, and β is the phase-accumulation in the light traveling in the dielectric layer. The total enhancement factor reaches the maximum value of 4 when β is $\pi/2$ and a perfect electrical conductor is used as the mirror that equates r_{23} to −1. Thus, the reflection coefficient for the mirror layer must be as close as possible to that of a perfect electrical conductor for the maximum enhancement factor. High reflectance from the mirror layer also assures that the absorbance/emissivity of the surface without an emitter layer is low, enhancing the contrast between the IR emissions with and without an emitter layer. In the IR wavelength range of interest (7 to 14 μm), that is the typical sensitivity range of thermal cameras, Al, Au, and

**ADVANCED
SCIENCE NEWS**

www.advancedsciencenews.com
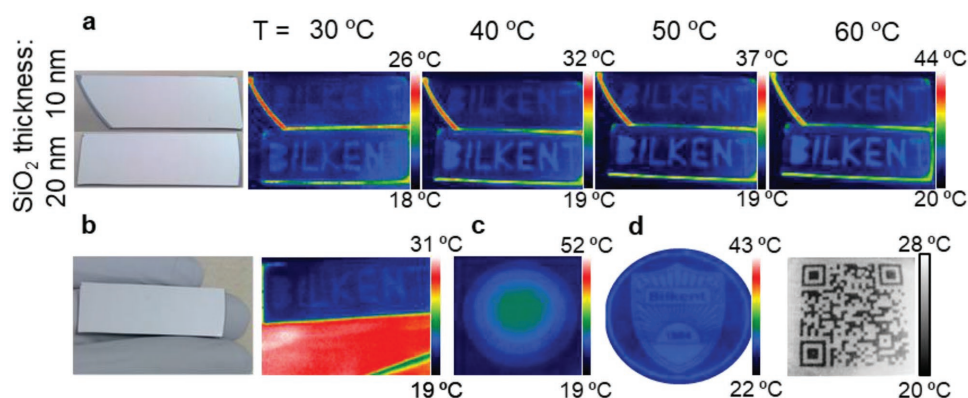
**ADVANCED
OPTICAL
MATERIALS**

www.advopticalmat.de

Figure 2. Designing the thermal emitter surfaces. a) Simulated electric field intensity enhancement factors on the dielectric surface for 1772 nm CaF_2, 914 nm ZnSe, and 661 nm amorphous Si on Al. The peak enhancement and the enhancement bandwidth are the largest for CaF_2, a low refractive index IR-transparent material. The dielectric film thicknesses are adjusted to maximize the field enhancement at $\lambda = 9$ µm. b) Simulated reflectance for CaF_2/Al, ZnSe/Al, and a-Si/Al surfaces. The peak absorbance/emissivity for bare CaF_2/Al surface is calculated to be ≈2% in the wavelength range of 7–13 µm, whereas it can reach up to 14% for bare a-Si/Al surface. The refractive indices of the dielectric layers are shown in Figure S5 (Supporting Information). Measured c) absorbance spectra in the infrared and d) reflectance spectra in the visible for SiO_2 layers with varying thickness on the field enhancement surface. Color map and plots share the same x-axis. e) Photograph and thermal images of SiO_2 patches with varying thickness on the field-enhancement surface at elevated temperatures. The patches are formed using a shadow mask and multiple deposition steps. Patch dimensions are 0.5×0.5 cm^2. f) Calculated emission spectra for a blackbody (dashed lines) and 10 nm SiO_2 on the field-enhancement surface (solid lines) for the temperature range of 30–60 °C. Emission from 10 nm SiO_2 is scaled by a factor of 3 for clarity.

Ag have the highest reflectance among other metals (Figure S2, Supporting Information). Thus, Al is chosen as the mirror layer due to its high reflectance in the mid IR and its low cost.

The final stage of the design is choosing the dielectric layer. The most important requirement is being lossless (transparent) in the infrared regime. Commonly used infrared-transparent dielectrics such as CaF_2, ZnSe, and Si are considered for this study. The field intensity enhancement factor is maximized for low refractive-index dielectrics such as CaF_2 when the mirror layer is not a perfect electrical conductor but an actual metal (**Figure 2**a). Furthermore, the bandwidth of the electric field

enhancement is the broadest for the material with the lowest refractive index, allowing more tolerance to thickness variations. More importantly, absorption of the incident IR light by the metal layer is lower for low refractive-index dielectrics due to the reduced interaction between the light and the metal layer (Figure 2b, Figures S3 and S4, Supporting Information). The enhanced light-metal interaction results in larger thermal emission from the bare surfaces and worsens the thermal intensity contrast between the background and absorber patterns (Figures S6 and S7, Supporting Information). As a result, CaF_2 is chosen as the dielectric material. The approximate

**ADVANCED
SCIENCE NEWS**

www.advancedsciencenews.com

**ADVANCED
OPTICAL
MATERIALS**

www.advopticalmat.de

Figure 3. Decrypting patterns in the IR. a) Photographs and thermal images of 10 and 20 nm-thick SiO$_2$ patterns spelling "BILKENT" on the field-enhancement surfaces. The letter heights are ≈1 cm. b) Photograph and thermal image of the sample with 20 nm SiO$_2$ using the external temperature of the human body. c) Thermal image with 2-bit color depth taken at 60 °C. SiO$_2$ thickness for the most outer ring is 5 nm and increases with 5 nm steps toward the center. d) Thermal images of SiO$_2$ patterns in the shape of the Bilkent University's logo and a QR code on field-enhancement surfaces. The thermal images are taken at 50 °C. The QR code image is taken in black and white and has enhanced contrast and brightness to be able to scan it using a QR scanner app. The sample sizes are ≈3 × 3 cm^2.

dielectric thickness is determined as $\lambda_{peak}/4n_d$, where λ_{peak} is the peak-enhancement wavelength, and n_d is the refractive index of the dielectric layer. The thickness is found as ≈1.8 µm for λ_{peak} = 9 µm using numerical simulations (Figure S8, Supporting Information). As a result, the peak absorbance for atop 10 nm thick SiO$_2$ is maximized for ≈1.8 µm thick CaF$_2$. The absorbance by the SiO$_2$ layer decreases for any other CaF$_2$ thickness (Figures S9 and S10, Supporting Information). The peak absorbance calculated for 10 nm SiO$_2$ on the field-enhancement surface is ≈4 times greater than what is calculated for the same layer suspended in air, following the field-intensity enhancement factor (Figure S1c vs Figure S9, Supporting Information). The final structure is similar to that is designed by Zhen et al.[18] that is 70 nm Si$_3$N$_4$ on 700 a-Si on Al. Zhen et al. has designed their surface to maximize the IR absorbance/emissivity in the wavelength range of 8–13 µm (that is the atmospheric transmittance window) for enhanced passive-cooling applications, hence the use of a-Si, instead of CaF$_2$, and 70 nm thick Si$_3$N$_4$ as the emitter instead of nanometer-thick SiO$_2$. In the rest of the text, 1.8 µm thick CaF$_2$-coated Al mirrors are referred to as the field-enhancement surfaces.

The maximum SiO$_2$ thickness that stays invisible on the field-enhancement surface is determined by experimenting SiO$_2$ thickness in the range of 10–50 nm. The thickest SiO$_2$ film maximizes the thermal emission (Figure S11 in the Supporting Information, Figure 2c). The visible reflectance spectra of the surfaces show interference fringes due to the thick CaF$_2$ that redshift with additional SiO$_2$ layers (Figure 2d). The shift in the reflectance spectra is noticeable for SiO$_2$ films thicker than 20 nm (Figure 2e). Thus, the SiO$_2$ thickness is chosen to be 20 nm or lower to hide, or encrypt, the patterns in the visible. The thermal emission from 20 nm thick SiO$_2$ patch can be distinguished from the background emission at 30 °C. Emissivity of the surfaces multiplied by the blackbody emission spectrum determines the thermal emission from the surfaces (Figure 2f). Hence, the thermal emission from 10 nm-thick SiO$_2$ patch shows a clear contrast with the background for increasing surface temperature, despite being not clear at 30 °C. Elevating the surface temperature is useful when the emitter layer is

preferred to be extremely thin, such as 5 nm. Such emitter thicknesses may be required to tolerate the variations in the optical behavior of the field-enhancement surfaces when alternative materials are used, e.g., transparent conductive oxides as the mirror layer.

2.2. Revealing SiO$_2$ Patterns in the IR

The lateral dimensions of the SiO$_2$ patterns must be macro-scale to be imaged by an ordinary thermal camera without any magnification. The SiO$_2$ patterns are fabricated by stencil method using laser-cut acetate shadow masks. The field-enhancement surfaces are produced by blanket deposition of Al and CaF$_2$ layers on 4″ silicon wafers and can potentially be produced on larger areas. Therefore, using the stencil method to form SiO$_2$ patterns makes the whole production process large-area fabrication compatible. The stencil method can also create fine patterns (with 10 µm resolution) using electroformed ultrathin metal shadow masks if needed. Such features, however, may not be captured by ordinary thermal cameras. The surfaces are imaged on a hot plate covered with Al foil to block the IR emission from the plate. Thermal images of SiO$_2$ patterns are observed to be noticeable starting at ≈30 °C for 20 nm thickness and ≈40 °C for 10 nm thickness. The emission contrast between the patterns and the background increases with increasing surface temperature for both surfaces (**Figure 3**a). Revealing the emitter patterns at a lower temperature enables the use of the human body as the heat source (Figure 3b). Using the surrounding that is a few degrees hotter than room temperature as the heat source reduces the thermal imaging setup to only a thermal camera. The thermal camera requirements such as resolution and field of view depend on the resolution and size of the patterns. The images used in this study have critical lateral dimensions on the order of millimeters and have overall sizes of centimeters. Such dimensions are found suitable for the stencil method and as well as thermal imaging of the patterns using a low-cost, smartphone-attachment-type thermal camera with a detector
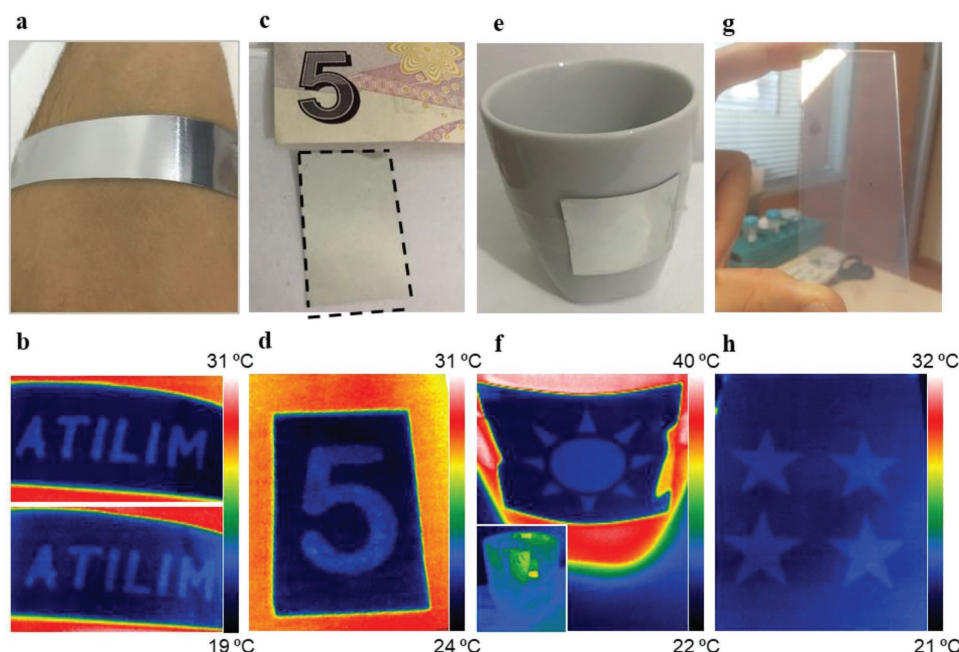
Figure 4. Alternative mirror layers. a) Photograph and b) thermal image of 50 nm thick SiO_2 patterns on 1.8 µm CaF_2-coated Al foil wrapped around an arm. Thermal images taken before (top) and after (bottom) laminating the foil with a polyethylene film. c) Photograph of a banknote and Al foil substrate (encircled with dashed frame) laminated on a piece of paper. The pattern is generated with 50 nm thick SiO_2. d) The laminated Al foil on paper is wrapped around an arm for thermal imaging. e) Photograph and f) thermal image of 40 nm thick SiO_2 patterns on the field-enhancement surface based on plastic substrate adhered on a mug. Thermal imaging is performed when the mug is empty (inset) and filled with water at 40 °C. The empty mug reflects the thermal emission coming from objects around it. Video S2 (Supporting Information) shows emergence of the thermal image as the mug is filled with hot water. g) Photograph and h) thermal image of 5 nm thick SiO_2 patterns on 1.8 µm CaF_2-coated FTO glass. The thermal image in (h) is taken at 60 °C.

matrix size of 206 × 156 pixels. The patterns that are created with single SiO_2 deposition step have 1-bit color depth (that is two colors) as shown by Figure 3a,b. Patterns with higher color depth can be created by sequential deposition steps to achieve various SiO_2 thicknesses (Figure 3c). If required, the thermal emission from the patterns can also be hidden by covering the surfaces with materials exhibiting strong IR absorbance like polydimethylsiloxane (PDMS) or water. The thermal emission can be concealed permanently by curing PDMS on the surfaces or temporary by simply wetting the surfaces (Figure S12, Supporting Information).

For high resolution SiO_2 images, optical lithography is employed. This approach is demonstrated by patterning a photoresist layer on the enhancement surface in the shape of Bilkent University's logo and a QR code followed by depositing 10 nm SiO_2 and lifting off the remaining photoresist (Figure 3d). For a clear contrast between the fine SiO_2 features and the background, the surface temperature is brought to 50 °C for thermal imaging. The QR code is recognized at lower temperatures, but it can only be scanned by the QR code app at elevated temperatures and with enhanced brightness and contrast (Figure S13, Supporting Information).

2.3. Alternative Mirror Layers

Switching to bendable substrates from rigid Si wafers is expected to enhance the versatility of applications. For this

task, Al foils are preferred as the bendable substrate as they are inherently low-cost, large area substrates that act like the support and as well as the mirror. The study of varying SiO_2 thickness is repeated for Al foils following deposition of 1.8 µm CaF_2. Visual inspection of the surface reveals that SiO_2 patterns as thick as 50 nm are imperceptible to the naked eye. The thicker SiO_2 patterns require only a few degrees above the room temperature to be detected in the thermal images (Figure S14, Video S1, Supporting Information). Al foil's flexibility and tolerance for thicker SiO_2 patterns allow wrapping the surfaces on body parts and thermal imaging of the surfaces using the body temperature (**Figure 4**a). The results demonstrate that thermal imaging of IR emitter patterns is possible on rough substrates after field enhancement (Figure 4b). In fact, for the application of detecting hidden IR emitter patterns, the rough substrates provide a better camouflage. The mechanical flexibility also enables covering the surface with wear-resistant films. As an example, the Al foil sample is laminated with tens of micrometers thick polyethylene film (Figure 4b). The choice of polyethylene over commonly preferred lamination material polyvinyl chloride (PVC) is based on the polyethylene's high transparency in the wavelength range of interest. Laminating Al foils also enables the use of arbitrary substrates like paper together with Al foils (Figure 4c,d). One advantage of using arbitrary substrates is the possibility of using the optical security features on banknotes which require many optical security features. Many of the modern banknotes already have metallic features that can also function as the mirror layer for
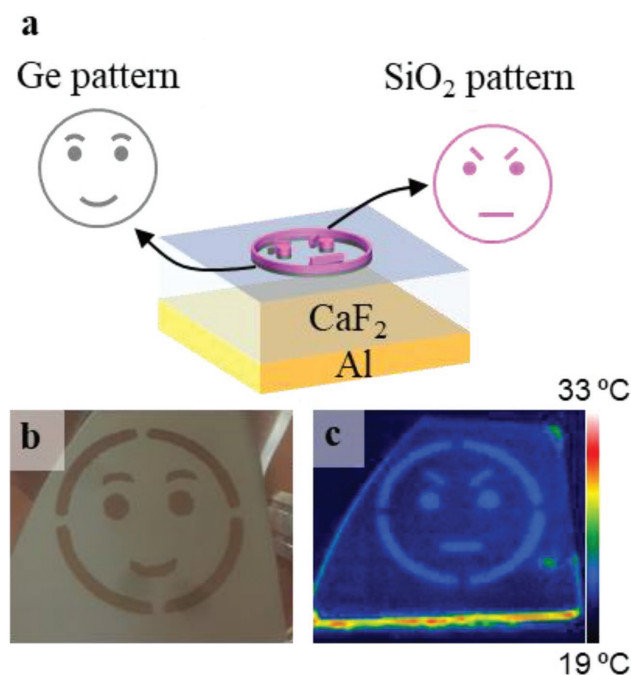
Figure 5. Storing different visual messages in the visible and infrared. a) 3D illustration of the field-enhancement surfaces surface with different patterns generated by 10 nm Ge and 10 nm SiO_2. b) Photograph of the surface. The text formed by 10 nm thick Ge is easily recognizable while the 10 nm thick SiO_2 layer is invisible. c) Thermal image of the surface revealing only the SiO_2 pattern at 40 °C.

a security feature using thermal emission. Plastic substrates can also serve as flexible enhancement surfaces after Al mirror and CaF_2 coating (Figure 4e,f). The maximum SiO_2 thickness that can be concealed on these substrates, however, is 40 nm. Another important observation is that the infrared absorption performance of the surfaces is unaffected while bending the substrate. This is a direct result of almost angle-independent absorbance/emissivity of the surfaces (Figure S15, Supporting Information).

Another alternative for the mirror layer is transparent conductive oxides that provide optical transparency in the visible while acting like a mirror in the IR (Figure 4g). Fluorine doped tin oxide (FTO) coated glasses are used for the study owing to their high electrical conductivity, hence high optical reflectance in the IR. Varying the SiO_2 thickness on 1.8 µm CaF_2-coated FTO glass reveals that the SiO_2 must be ≈5 nm to be imperceptible by the naked eye. The ultrathin SiO_2 layer reduces the thermal emission from the SiO_2 patterns. Furthermore, FTO exhibits greater absorbance/emissivity compared to the Al mirrors (Figure S16, Supporting Information). Thus, the infrared emission contrast between the SiO_2 patterns and the background is weaker for the FTO-based surfaces and can only be observed at higher temperatures (≈70 °C) (Figure 4h). Thin metal (Ag) films are also considered for this application. However, the Ag thicknesses required to achieve acceptable IR performance offer low transparency in the visible, hence overall performance of such surfaces is found inferior to that of the FTO glass substrates (Figure S17, Supporting Information).

2.4. Storing Different Messages in the Visible and Infrared

An alternative encryption mechanism is hiding an emitter pattern on top a different visible pattern. This functionality can be achieved using infrared-transparent materials like Ge that are lossy in the visible, hence perceptible by the naked eye. While determining the effect of the refractive index of the dielectric material on the IR performance of the surfaces, it is argued that high refractive-index dielectric materials like Ge increase the background IR emission. On the other hand, if the Ge layer is kept very thin, e.g., 10 nm, on the CaF_2 dielectric layer, the generated Ge patterns become visible while the IR emission is not significantly disturbed (Figure S18, Supporting Information). In this mode of operation, the patterns are perceptible by the naked eye and hidden in the infrared that is the opposite of what is demonstrated in the manuscript so far. Encryption is achieved when a different pattern is generated by a thin emitter layer. The patterns detected in the visible and the IR are then different (**Figure 5**). The performance of the surface is unaffected when the Ge layer is created above the SiO_2 pattern (Figure S19, Supporting Information). Alternatively, the silica coating can be present only some part of the visible pattern emphasizing those parts of the visible message in the IR (Figure S20, Supporting Information).

3. Discussion

The demonstrated encryption principle is based on materials that are lossless in the visible, but lossy in the infrared such as SiO_2. When such a material is coated as nanometer-thick patterns on an infrared-transparent substrate like ZnSe window, it would not be noticed by the naked eye, but would emit IR light. Thus, the pattern would be encrypted in the visible to be decrypted by thermal imaging, albeit requiring high surface temperatures to enhance the IR emission to the detectable levels. In this study, the IR emission from the thin film is enhanced by enhancing its emissivity/absorbance on a uniform field-enhancement surface, enabling decryption of the patterns for relatively low temperatures (Figure S21, Supporting Information). The absorbance enhancement on such a surface follows the electric-field intensity enhancement as described by the Beer's law.[37] Using Al as the mirror and CaF_2 as the dielectric layer provides an enhancement factor of 3.96 that is very close to the theoretical value of 4. This enhancement factor is much larger than the enhancement factors achieved on simple infrared transparent substrates being ≈0.75, ≈0.35, and ≈0.2 for CaF_2, ZnSe, and Si substrates, respectively, in the wavelength range of interest. As a result, the thermal emission from a 10 nm thick SiO_2 film on the field-enhancement surface at 300 K is barely matched by the same thickness SiO_2 film on a CaF_2 substrate at 450 K, which is an impractical temperature for the proposed application (Figure S21, Supporting Information). While the absorber/dielectric/metal structure is kept constant, alternative materials are considered, especially for the metal layer and the substrate, to demonstrate the adaptability of the surfaces (Table S1, Supporting Information).

The field-enhancement can also be achieved using plasmonic structures[38] or photonic crystals,[39] both of which necessitate

micromachining, challenging the large-area fabrication, hence the ability to use low-cost thermal cameras without magnification. Furthermore, the extreme, but yet, spatially localized field enhancements on such surfaces result in infrared absorbance by the absorber layer comparable to what is observed on the uniform-field enhancement surfaces.[40,41] Another disadvantage of such surfaces would be the increased background thermal emission that would worsen the contrast in thermal images. As a result, the uniform field-enhancement surfaces are preferred over the alternatives like plasmonic structures and photonic crystals.

The optical encryption–decryption function demonstrated in this study exploits the large-area fabrication techniques, low-cost and flexible substrates and a convenient decryption method. These features are superior to those of recently reported alternatives that have either small areas[33–36,42] or involved encryption/decryption methods.[26,43] Table S2 (Supporting Information) lists these alternatives and compares them to this study.

4. Conclusion

The results, especially the demonstration of large-area, flexible/bendable substrates, are promising for the potential use of the proposed operation for anticounterfeit applications such as enhancing the optical security features of banknotes.

5. Experimental Section

Fabrication: Al was thermally evaporated on Si or plastic substrates at ≈10^{-6} Torr at a rate of ≈2 Å s^{-1}. CaF_2 was thermally evaporated in the same chamber at a rate of ≈20 Å s^{-1}. CaF_2 was e-beam evaporated on Al-coated plastic substrate. Ge was thermally evaporated on field-enhancement surfaces at a rate of 0.5 Å s^{-1}. Ge was also deposited as an adhesion layer on plastic substrate prior to Al deposition. SiO_2 was e-beam evaporated on the field enhancement surfaces at a rate of ≈2 Å s^{-1}. SiO_2 patterns were formed using laser-cut plastic shadow masks. The fine patterns in Figure 4 were achieved using optical lithography and lift-off as described here: The field-enhancement surfaces on Si were spin-coated with ≈1.4 µm thick AZ5214E photoresist (4000 rpm, 50 s). The surfaces were prebaked at 110 °C for 50 s and exposed with 60 mJ UV-light using a mask aligner (EVG 620). The photoresist was developed in AZ developer/DI water solution (1:4 v/v) for 1 min. The remaining photoresist was lifted-off using acetone following the SiO_2 deposition. FTO-coated-glasses were purchased from Solarix.

Preparation of Stencils: 150 µm thick clear acetate sheets were laser-cut as stencils. The patterns were created using a CAD software then transferred to a CO_2 laser (Epilog, Zing). Laser operated at 10.6 µm of wavelength, maximum output power of 30 W and frequency of 5 kHz with two different cutting modes of raster engraving and vector cutting. The following parameters were used for CO_2 laser cutting: Vector cutting mode, 1000 DPI resolution, 4.5 W output power, 5 kHz frequency, ≈100 µm beam diameter, and 2.6 cm s^{-1} speed during acetate cutting.

Measurements: Reflection and transmission measurements in the visible and infrared were performed using ellipsometers (J.A. Woollam Co., V-Vase and J.A. Woollam Co., IR-Vase). Thermal images were taken with a Seek Compact thermal camera. Key features of the camera were sensor array size of 206 × 156 pixels, 36° of field of view, spectra range of 7.5–14 µm, and focusable lens. The photographs were taken with an iPhone 7.

Simulations: Transfer matrix method was employed to calculate the reflectance, transmittance, and absorbance of surfaces. The refractive index (n) and the extinction coefficient (k) of CaF_2 and SiO_2 that are used in the simulations are characterized using varying-angle spectroscopic ellipsometer measurements. Palik data were used for the metals.

Supporting Information

Supporting Information is available from the Wiley Online Library or from the author.

Conflict of Interest

The authors declare no conflict of interest.

[1] A. Lenert, D. M. Bierman, Y. Nam, W. R. Chan, I. Celanovic, M. Soljacic, E. N. Wang, *Nat. Nanotechnol.* **2014**, *9*, 126.

[2] O. Ilic, P. Bermel, G. Chen, J. D. Joannopoulos, I. Celanovic, M. Soljačić, *Nat. Nanotechnol.* **2016**, *11*, 320.

[3] K. A. Arpin, M. D. Losego, A. N. Cloud, H. Ning, J. Mallek, N. P. Sergeant, L. Zhu, Z. Yu, B. Kalanyan, G. N. Parsons, G. S. Girolami, J. R. Abelson, S. Fan, P. V. Braun, *Nat. Commun.* **2013**, *4*, 2630.

[4] A. P. Raman, M. A. Anoma, L. Zhu, E. Rephaeli, S. Fan, *Nature* **2014**, *515*, 540.

[5] P.-C. Hsu, A. Y. Song, P. B. Catrysse, C. Liu, Y. Peng, J. Xie, S. Fan, Y. Cui, *Science* **2016**, *353*, 1019.

[6] B. Temelkuran, S. D. Hart, G. Benoit, J. D. Joannopoulos, Y. Fink, *Nature* **2002**, *420*, 650.

[7] A. Yildirim, M. Vural, M. Yaman, M. Bayindir, *Adv. Mater.* **2011**, *23*, 1263.

[8] A. Lochbaum, Y. Fedoryshyn, A. Dorodnyy, U. Koch, C. Hafner, J. Leuthold, *ACS Photonics* **2017**, *4*, 1371.

[9] A. Mech, A. Monguzzi, F. Meinardi, J. Mezyk, G. Macchi, R. Tubino, *J. Am. Chem. Soc.* **2010**, *132*, 4574.

[10] T. Asano, M. Suemitsu, K. Hashimoto, M. De Zoysa, T. Shibahara, T. Tsutsumi, S. Noda, *Sci. Adv.* **2016**, *2*, e1600499.

[11] Y. Zhai, Y. Ma, S. N. David, D. Zhao, R. Lou, G. Tan, R. Yang, X. Yin, *Science* **2017**, *355*, 1062.

[12] A. Srinivasan, B. Czapla, J. Mayo, A. Narayanaswamy, *Appl. Phys. Lett.* **2016**, *109*, 061905.

[13] J. Kou, Z. Jurado, Z. Chen, S. Fan, A. J. Minnich, *ACS Photonics* **2017**, *4*, 626.

[14] J. Drevillon, K. Joulain, P. Ben-Abdallah, E. Nefzaoui, *J. Appl. Phys.* **2011**, *109*, 034315.

[15] T. Wang, P. Li, D. N. Chigrin, A. J. Giles, F. J. Bezares, O. J. Glembocki, J. D. Caldwell, T. Taubner, *ACS Photonics* **2017**, *4*, 1753.

[16] H. Kocer, S. Butun, Z. Li, K. Aydin, *Sci. Rep.* **2015**, *5*, 8157.

[17] H. Kocer, S. Butun, E. Palacios, Z. Liu, S. Tongay, D. Fu, K. Wang, J. Wu, K. Aydin, *Sci. Rep.* **2015**, *5*, 13384.

[18] Z. Chen, L. Zhu, A. Raman, S. Fan, *Nat. Commun.* **2016**, *7*, 13729.

[19] V. W. Brar, M. C. Sherrott, M. S. Jang, S. Kim, L. Kim, M. Choi, L. A. Sweatlock, H. A. Atwater, *Nat. Commun.* **2015**, *6*, 7032.

[20] W. Streyer, S. Law, G. Rooney, T. Jacobs, D. Wasserman, *Opt. Express* **2013**, *21*, 9113.

[21] M. A. Kats, D. Sharma, J. Lin, P. Genevet, R. Blanchard, Z. Yang, M. M. Qazilbash, D. N. Basov, S. Ramanathan, F. Capasso, *Appl. Phys. Lett.* **2012**, *101*, 221101.

[22] M. A. Kats, R. Blanchard, S. Zhang, P. Genevet, C. Ko, S. Ramanathan, F. Capasso, *Phys. Rev. X* **2013**, *3*, 041004.

[23] H. Sai, H. Yugami, *Appl. Phys. Lett.* **2004**, *85*, 3399.

[24] M. U. Pralle, N. Moelders, M. P. McNeal, I. Puscasu, A. C. Greenwald, J. T. Daly, E. A. Johnson, T. George, D. S. Choi, I. El-Kady, R. Biswas, *Appl. Phys. Lett.* **2002**, *81*, 4685.

[25] X. Liu, T. Tyler, T. Starr, A. F. Starr, N. M. Jokerst, W. J. Padilla, *Phys. Rev. Lett.* **2011**, *107*, 045901.

[26] M. Makhsiyan, P. Bouchon, J. Jaeck, J.-L. Pelouard, R. Haïdar, *Appl. Phys. Lett.* **2015**, *107*, 251103.

[27] E. Rephaeli, A. Raman, S. Fan, *Nano Lett.* **2013**, 130311121615001.

[28] O. Salihoglu, H. B. Uzlu, O. Yakar, S. Aas, O. Balci, N. Kakenov, S. Balci, S. Olcum, S. Süzer, C. Kocabas, *Nano Lett.* **2018**, *18*, 4541.

[29] M. De Zoysa, T. Asano, K. Mochizuki, A. Oskooi, T. Inoue, S. Noda, *Nat. Photonics* **2012**, *6*, 535.

[30] T. Inoue, M. De Zoysa, T. Asano, S. Noda, *Nat. Mater.* **2014**, *13*, 928.

[31] K.-K. Du, Q. Li, Y.-B. Lyu, J.-C. Ding, Y. Lu, Z.-Y. Cheng, M. Qiu, *Light: Sci. Appl.* **2016**, *6*, e16194.

[32] G. Bakan, S. Ayas, E. Ozgur, K. Celebi, A. Dana, *ACS Sensors* **2016**, *1*, 1403.

[33] Y. Cui, R. S. Hegde, I. Y. Phang, H. K. Lee, X. Y. Ling, *Nanoscale* **2014**, *6*, 282.

[34] F. Yue, C. Zhang, X. Zang, D. Wen, D. B. Gerardot, S. Zhang, X. Chen, *Light: Sci. Appl.* **2017**, *6*, e17066.

[35] Q. Dai, M. Ouyang, W. Yuan, J. Li, B. Guo, S. Lan, S. Liu, Q. Zhang, G. Lu, S. Tie, H. Deng, Y. Xu, M. Gu, *Adv. Mater.* **2017**, 1701918.

[36] X. Duan, S. Kamin, N. Liu, *Nat. Commun.* **2017**, *8*, 14606.

[37] S. Ayas, G. Bakan, E. Ozgur, K. Celebi, A. Dana, *ACS Photonics* **2016**, *3*, 337.

[38] C. Ciracì, R. T. Hill, J. J. Mock, Y. Urzhumov, A. I. Fernández-Domínguez, S. A. Maier, J. B. Pendry, A. Chilkoti, D. R. Smith, *Science* **2012**, *337*, 1072.

[39] N. Ganesh, W. Zhang, P. C. Mathias, E. Chow, J. A. N. T. Soares, V. Malyarchuk, A. D. Smith, B. T. Cunningham, *Nat. Nanotechnol.* **2007**, *2*, 515.

[40] C. Huck, A. Toma, F. Neubrech, M. Chirumamilla, J. Vogt, F. De Angelis, A. Pucci, *ACS Photonics* **2015**, *2*, 497.

[41] J. M. Hoffmann, H. Janssen, D. N. Chigrin, T. Taubner, *Opt. Express* **2014**, *22*, 14425.

[42] J. Xue, Z.-K. Zhou, Z. Wei, R. Su, J. Lai, J. Li, C. Li, T. Zhang, X.-H. Wang, *Nat. Commun.* **2015**, *6*, 8906.

[43] C. Zhang, B. Wang, W. Li, S. Huang, L. Kong, Z. Li, L. Li, *Nat. Commun.* **2017**, *8*, 1138.